

Contents lists available at ScienceDirect

International Journal of Plasticity

journal homepage: www.elsevier.com/locate/ijplas





Achieving strength and ductility synergy via a nanoscale superlattice precipitate in a cast Mg-Y-Zn-Er alloy

Mingyu Fan ^a, Zhongwu Zhang ^{a,*}, Ye Cui ^{a,*}, Liyuan Liu ^a, Yingwei Liu ^a, Peter K. Liaw ^{b,*}

ARTICLE INFO

Keywords:
Cast Mg alloys
Mechanical property
Er addition
Nanoscale superlattice precipitates
Dislocations

ABSTRACT

Precipitation strengthening is one of the most promising methods to develop magnesium (Mg) alloys. However, the nerve-wracking fact is that the cast Mg alloys always have coarse second particles, which inevitably leads to a poor ductility. In this study, a novel nanoscale superlattice precipitate (NSP) with a superior strengthening effect is developed by rare-earth Er alloying. The newly-developed cast Mg-Y-Zn-Er alloy possesses a yield strength of 154 MPa, a tensile strength of 234 MPa, and a total elongation of $\sim 13\%$. The NSPs is systematically investigated, using transmission electron microscopy and first-principles calculations. The NSP with an average radius of 4 nm has a five periodic supercell structure enriched with Zn, Y, and Er atoms. The first-principles calculations indicate that Zn, Y, and Er atoms are apt to segregate on the (11 $\overline{2}1$) plane. The excellent strength is contributed mainly by the ordering strengthening of the NSPs. The addition of Er enhances the multiplication of dislocations and the activation of $\langle c+a\rangle$ dislocation system during deformation, contributing to the ductility.

1. Introduction

Cast Mg alloys offer significant potential use in aerospace and vehicles due to their low density, short processing cycles, low assembly costs, tremendous design flexibility and opportunities for part integration, compared with wrought Mg alloys (Agnew and Nie, 2010; Pan et al., 2016). Among many cast Mg alloys, cast Mg rare-earth alloys has attracted extensive attention due to their high strength, creep resistances, good ignition proof ability and corrosion resistance (Wu et al., 2021). Precipitation strengthening (Wu et al., 2021) is one of the main methods to improve the strength for cast Mg rare-earth alloys. In particular, the long-period stacking-ordered (LPSO) phase provides superb strength and ductility via hindering the dislocation movement (Guo et al., 2020; Mayama et al., 2022) and activating the non-basal slip of Mg alloys (Agnew et al., 2018; Kim et al., 2015). It has been reported that LPSO structures were observed in Mg-Zn-RE (the rare-earth elements, RE = Y, Tb, Dy, Ho, and Er) systems. RE-Mg and Zn-RE have the negative mixing enthalpy and hexagonal close-packed (HCP) structure at room temperature. The solid solubility of these REs in the Mg matrix is greater than 3.75 atomic percent (at%) and the difference in atomic sizes between REs and Mg is greater than 8.4 to 11.9% (Xu et al., 2016). All these aspects of REs are beneficial to the formation of LPSO. However, although the LPSO phase greatly improves

E-mail addresses: zwzhang@hrbeu.edu.cn (Z. Zhang), cuiye@hrbeu.edu.cn (Y. Cui), pliaw@utk.edu (P.K. Liaw).

^a Key Laboratory of Superlight Materials and Surface Technology, Ministry of Education, College of Materials Science and Chemical Engineering, Harbin Engineering University, Harbin 150001, China

b Department of Materials Science and Engineering, The University of Tennessee, Knoxville, TN 37996-2100, United States

^{*} Corresponding authors.

the mechanical properties of wrought Mg alloys, it shows poor combination of strength and ductility in cast Mg rare-earth alloys (Cheng et al., 2018). In cast Mg rare-earth alloys, the LPSO phase or RE-rich phase are always too coarse to eliminate in the subsequent heat treatment (Liao et al., 2020; Lu et al., 2015). Most of the coarse second phases, such as RE-, Ca- and Si- containing phases, often induce brittleness upon deformation since micro-cracks could be generated by the decohesion of matrix/particle interface or fracture of particles (Jin et al., 2022). Therefore, minimizing and dispersing second phases via twin-roll casting (Zhang et al., 2021b) and increasing cooling rate (Jin et al., 2021) in Mg alloys have been extensively investigated. However, it is still a great challenge to further improve the strength and ductility of cast Mg.

It is reported (Jiang et al., 2017; Xu et al., 2019) that a coherent nanoscale precipitates-enhanced steel can exhibit high strength without the loss of ductility since nanoscale precipitates hinder the slip of dislocations through shearing mechanisms. In maraging steels, the alloy strength can reach 2.2 GPa by introducing high-density coherent nanoscale precipitates (Jiang et al., 2017). Based on the theory of the dislocation-shearing mechanism, the uniformly-distributed high-density nanoscale precipitates reduce the stress concentration to prevent crack initiations at the interface between the nanoscale precipitates and the matrix (Jiang et al., 2017). Thus, it is expected to obtain excellent strength without loss of ductility by introducing the coherent nanoscale precipitates into Mg alloys.

Erbium (Er) is a kind of heavy rare-earth elements, which satisfies the formation criteria of the LPSO structure in Mg alloys (Xu et al., 2016). Furthermore, the Er element has a large solid solubility [32.7 wt percent (wt%)] at the eutectic temperature) in Mg matrix and has a larger atomic radius (1.76 Å) than Mg (1.60 Å), Therefore, the dissolve of element Er in Mg will cause the Mg lattice expansion. The Zn element dissolving in Mg will cause the Mg lattice to shrink due to the smaller atomic radius (1.39 Å). Thus, the easily formed Er-Zn pairs (Takeuchi and Inoue, 2005; Zhang et al., 2010) can cause the least lattice distortion and the elastic strain energy, reducing the precipitation resistance.

In this paper, we develop a method to improve the yield strength of a cast Mg alloy without the loss of ductility by introducing NSPs through the addition of the elements of Er, Y and Zn. The influence of Er on the microstructures, including the formation of the LPSO phase, W phase, and NSPs, is characterized systematically. The effects of LPSO phase, W phase, and NSPs on the mechanical properties are studied and discussed in detail.

2. Material and methods

The alloys with a nominal composition (at%) of $Mg_{98}Y_1Zn_1$ and $Mg_{97.5}Y_1Zn_1Er_{0.5}$ were fabricated from the pure Mg (99.99 wt%), pure Zn (99.9 wt%), Mg-Er (20 wt%) master alloy, and Mg-Y (20 wt%) master alloy. The alloys were melted in an electric resistance furnace equipped with a steel crucible under a mixed atmosphere of CO_2 and SF_6 and then cast into steel mold. The tensile tests were performed on an Instron 5869 testing machine at a strain rate of $1 \times 10^{-3} \, s^{-1}$. The tensile specimens were strip-like with a strain gage size of $12.5 \, \text{mm} \times 4 \, \text{mm} \times 1 \, \text{mm}$. Hardness measurements were conducted on an HXS-1000Z tester under an applied load of 25 g for $15 \, s$. An average of at least $15 \, \text{times}$ measurements for each sample was reported.

The scanning electron microscopy (SEM, APREO SLOVAC) was used to analyze the grain size and phase-volume fraction. The electron backscatter diffraction (EBSD) measurements were carried out on a scanning electron microscope (SEM zeiss ultra55) equipped with oxford nordlysNano by a step size of $1.7~\mu m$. The EBSD data were analyzed by the AZtecCrystal. The TEM samples were prepared by punching 3-mm diameter discs with 30 μm in thickness and low-angle (3° - 9°) ion milling, using a Gatan 695 precision argon-ion polishing system and focused ion beam (FIB) milling system (FEI LD Helios G5 UX). The ion-milling samples were analyzed on the transmission electron microscopy (TEM, FEI Talos F200X G2), which reveal the structures of the LPSO phase, the nanoscale superlattice precipitates, dislocation configurations and interaction between dislocations and nanoscale superlattice precipitates. FIB sample with a thickness of 50 nm was used to analyze elemental distribution and volume fraction of nanoscale superlattice precipitates by the transmission electron microscopy (FEI Themis Z) with spherical aberration correctors. The volume fraction of the NSPs is estimated as

$$f = \frac{\frac{4}{3}\pi r^3 N}{LWT} \tag{1}$$

The f represents the volume fraction of the NSPs, r is the average radius of NSPs, N is the number of NSPs in the selected area, L, W and T are length, width and thickness (50 nm) in the selected area, respectively. At least ten images were conducted in order to ensure the statistics of the volume fraction of NSPs. Phase identification was performed, utilizing X-ray diffraction on an X'Pert Pro-X diffractometer employing Cu K_{α} . ($\lambda=0.15406$ nm). The diffraction lines were recorded at 40 kV and 150 mA from 20 to 80° with a step of 0.02° (2θ).

The quantitative analyses of dislocation densities were performed, based on the XRD data of the tested tensile samples, using the Williamson-Hall method (Fu et al., 2022; Williamson and Hall, 1953). For this technique, the following mathematical relation is employed to relate the integral breadth (β), average domain size (D_{ν}), and the microstrain (ε), and is given by Shahbeigi Roodposhti et al. (2015):

$$\frac{\beta cos\theta}{\lambda} = \frac{1}{D_V} + 2\varepsilon \left(\frac{2Sin\theta}{\lambda}\right) \tag{2}$$

where λ is the wavelength (0.154 nm for Cu K_{α}), and θ is the Bragg angle. The regression analysis of the plot for β cos / λ vs. 2sin θ / λ gives the values of ε and D_V , from the slope and the ordinate intersection, respectively. The dislocation density, ρ , is calculated by analyzing the micro-strain through the following equation (Williamson and Smallman, 1956):

Fig. 1. (a) Engineering tensile stress-strain curves of the $Mg_{98}Y_1Zn_1$ and $Mg_{97.5}Y_1Zn_1Er_{0.5}$ alloys, (b) Comparison of the tensile strength and elongation of the cast $Mg_{97.5}Y_1Zn_1Er_{0.5}$ alloys (cheng et al., 2018; He, 2007; Kawamura et al., 2006; Li et al., 2013; Luo et al., 2019; Okayasu et al., 2016; Wang et al., 2010; Yang et al., 2017; Zhang et al., 2014).

$$\rho = \frac{k\varepsilon}{L^2} \tag{3}$$

where *k* is the material constant (considered as 1 for magnesium alloys (Shahbeigi Roodposhti et al., 2015)), and *b* is the magnitude of the Burger's vector [considered as 0.32 nm for magnesium alloys (Zhang et al., 2017a)].

Energetics and atomic occupation of nanoscale precipitates were calculated with the Materials Studio 8.0. The generalized gradient approximation (GGA) of Perdew–Burke–Ernzerhof (PBE) (Guo et al., 2020) was selected as the exchange-correlation function. Three dimensional 60-atom periodic supercells are utilized to calculate the total energy, using the $2 \times 4 \times 3$ Monkhorst–Pack mesh with a plane-wave cut-off energies of 400 eV.

3. Results

3.1. Mechanical properties

The representative engineering stress-strain curves in tension for the as-cast $Mg_{98}Y_1Zn_1$ and $Mg_{97.5}Y_1Zn_1Er_{0.5}$ samples are shown in Fig. 1(a). The tensile yield strength of $Mg_{97.5}Y_1Zn_1Er_{0.5}$ is ~ 154 MPa, which is 2 times higher than 77 MPa for the $Mg_{98}Y_1Zn_1$ alloy. The ductility of $Mg_{97.5}Y_1Zn_1Er_{0.5}$ remains the same (13%) as the counterpart without the Er addition though the strength is enhanced significantly. Moreover, the strength increase corresponding to the work-hardening stage is not affected by the addition of Er, as presented in Fig. 1(a). The as-cast $Mg_{97.5}Y_1Zn_1Er_{0.5}$ alloy possesses a high tensile strength of 234 MPa, a yield strength of 154 MPa, and an elongation of 13%, which is superior to most of the reported results for as-cast Mg alloys (Cheng et al., 2018; He, 2007; Kawamura et al., 2006; Li et al., 2013; Luo et al., 2019; Okayasu et al., 2016; Wang et al., 2015, 2010; Yang et al., 2017; Zhang et al., 2014), as shown in Fig. 1(b). It is obvious that the cast $Mg_{97.5}Y_1Zn_1Er_{0.5}$ alloys exhibit excellent tensile properties, which is comparable to that of complex Mg-4.0Y-2Nd-1.0Gd-0.5Zn-0.5Zr (wt.%) alloys.

3.2. Microstructures

Microstructures of the cast $Mg_{98}Y_1Zn_1$ and $Mg_{97.5}Y_1Zn_1Er_{0.5}$ alloys analyzed by EBSD are shown in Fig. 2(a) and 2(b). Both cast alloys have large grains, which are mainly composed of many fine effective grains with a similar crystal orientation. The fine effective grains in one large grain are separated by the second phases in a net-like structure. Also, no preferred orientation or textures can be observed even though the statistical number of grains are small due to the large grain size in the cast alloys. This is in agreement with

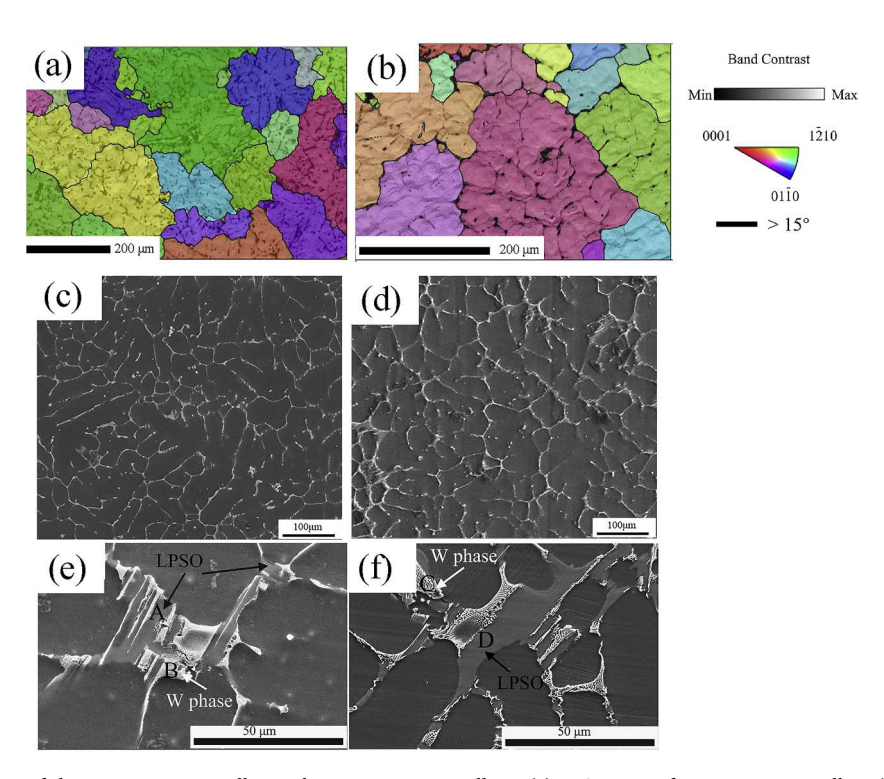


Fig. 2. Microstructures of the cast $Mg_{98}Y_1Zn_1$ alloy and $Mg_{97.5}Y_1Zn_1Er_{0.5}$ alloys. (a) EBSD map of cast $Mg_{98}Y_1Zn_1$ alloy, (b) EBSD map of cast $Mg_{98}Y_1Zn_1$ alloy, SEM microstructure images of (c) $Mg_{98}Y_1Zn_1$ alloy, (d) $Mg_{97.5}Y_1Zn_1Er_{0.5}$ alloy, high-magnified SEM images showing the second phases in (e) $Mg_{98}Y_1Zn_1$ alloy, (f) $Mg_{97.5}Y_1Zn_1Er_{0.5}$ alloy.

some previous results that there are no obvious texture in cast Mg alloys (Park et al., 2014; Stanford and Phelan, 2010). The SEM micrographs of the $Mg_{98}Y_1Zn_1$ and $Mg_{97.5}Y_1Zn_1Er_{0.5}$ alloys are shown in Fig. 2(c) and 2(d) to elucidate the phase constituents. It can be seen that both the $Mg_{98}Y_1Zn_1$ and $Mg_{97.5}Y_1Zn_1Er_{0.5}$ alloys are mainly composed of the dark Mg matrix and bright second phases, which is distributed in the matrix, creating continuous nets. Through the statistical analysis of the effective grain size, the average effective grain sizes of 41 μ m and 40 μ m can be determined for $Mg_{98}Y_1Zn_1$ and $Mg_{97.5}Y_1Zn_1Er_{0.5}$ alloys, respectively. The volume fractions of the second phases in $Mg_{98}Y_1Zn_1$ and $Mg_{97.5}Y_1Zn_1Er_{0.5}$ alloys were $\sim 11\%$ (LPSO phase: 9%; W phase: 2%), respectively.

In order to further identify the web-like second phases, high-magnification SEM micrographs are shown in Fig. 2(e) and 2(f). There are two kinds of second phases, i.e., gray region and white region, for both $Mg_{98}Y_1Zn_1$ and $Mg_{97.5}Y_1Zn_1Er_{0.5}$. The detailed elemental compositions of the gray and white regions determined by the X-ray energy-dispersive spectrometer (EDS) in $Mg_{98}Y_1Zn_1$ and $Mg_{97.5}Y_1Zn_1Er_{0.5}$ are summarized in Table 1. The atomic ratio of RE/Zn is close to 1:1, corresponding to the chemical composition of an LPSO phase in the gray phase, while it is close to that of the W phase (RE/Zn = 2:3) in the white phase. It is clear that the large grain size, the average effective fine grain size and the volume fraction of the second phase are not influenced by the addition of Er.

The XRD patterns for $Mg_{98}Y_1Zn_1$ and $Mg_{97.5}Y_1Zn_1Er_{0.5}$ alloys are displayed in Fig. 3. Based on the XRD analysis, the major phases in both alloys with and without Er are the α -Mg matrix, LPSO phase, and W phase, confirming that the second phases presented in Fig. 2 are the LPSO and W phases.

The bright-field TEM images of the LPSO and W phases for $Mg_{98}Y_1Zn_1$ and $Mg_{97.5}Y_1Zn_1Er_{0.5}$ alloys are shown in Fig. 4, and the corresponding SAED patterns of the LPSO and W phases are presented in the insets. In Fig. 4(a) and 4(b), it can be seen that there were five extra diffraction spots, appearing at the $\pm 1/6(0002)_{\alpha}$, $\pm 2/6(0002)_{\alpha}$ $\pm 5/6(0002)_{\alpha}$ positions (α represents the Mg matrix), of the $Mg_{98}Y_1Zn_1$ and $Mg_{97.5}Y_1Zn_1Er_{0.5}$ diffraction patterns (Kishida et al., 2015), confirming that the observed LPSO phase in both $Mg_{98}Y_1Zn_1$ and $Mg_{97.5}Y_1Zn_1Er_{0.5}$ alloys is the 18R LPSO phase. The structure of the W phase is shown in Fig. 4(c) and 4(d) for both two alloys. The corresponding selected area electron diffraction (SAED) pattern analysis (Fig. 4(c) and 4(d)) confirms that the W phase in both alloys is with the face-centered cubic (FCC) structure. The addition of Er did not affect the structures of the LPSO and W phases. Moreover, the microhardness of LPSO phase containing Er and without Er are 84 \pm 9 and 86 \pm 7HV, respectively. This results is close to the hardness of LPSO phase (92.3 \pm 2.3) reported by Lyu et al. (2020). The results imply the change of hardness of the LPSO phase can be negligible with the addition of Er.

The HAADF-TEM images for $Mg_{98}Y_1Zn_1$ and $Mg_{97.5}Y_1Zn_1Er_{0.5}$ alloys are shown in Fig. 5(a) and 5(b), respectively. It can be seen that there is a large amount of uniformly distributed nanoscale precipitates (white dots indicated by white arrows) in $Mg_{97.5}Y_1Zn_1Er_{0.5}$ alloys, as presented in Fig. 5(b). However, the nanoscale precipitates cannot be found in the $Mg_{98}Y_1Zn_1$ alloy, as shown Fig. 5(a). The results indicate that Er is the key to the formation of nanoscale precipitates. Fig. 6 presents a high-resolution (HR)-TEM image of the nanoscale precipitates, and the fast Fourier transformation (FFT) patterns. The inverse fast Fourier transformation (IFFT) images corresponding to the nanoscale precipitates are presented in Fig. 6(c). In the FFT pattern, as shown in Fig. 6(b), the nanoscale precipitates show four spots close to the primary beam (marked by the yellow arrows), indicating that a superlattice parallels to the substrate. To further examine the interfaces between the Mg matrix and NSPs, high-resolution TEM (HRTEM) was employed, as shown in Fig. 6(d). The lattice-parameter mismatch between the matrix and NSPs is estimated as 0.1% by the equation of $\eta = 2(\alpha_{NSPs} - \alpha_{matrix})/(\alpha_{NSPs} + \alpha_{matrix})$, where α is the respective lattice parameter. The result clearly shows a coherent interface between the NSPs and Mg matrix with the same atomic-arrangement direction and interplanar spacing.

The periodicity of the superlattice is 0.75 nm, which is about 5 times of the spacing of $\{11\overline{21}\}$ (0.15 nm), as shown in Fig. 7, indicating the five-periodic-supercell structure in the $(11\overline{2}1)$ plane of NSPs. The HAADF-TEM image and the corresponding elemental distribution of the NSPs in the cast $Mg_{97.5}Y_1Zn_1Er_{0.5}$ alloy are shown in Fig. 8. It is obvious that the precipitates are enriched with Er, Y and Zn atoms.

4. Discussion

4.1. Formation of nanoscale superlattice precipitates

Based on the TEM analysis, the NSPs have the five-periodic-supercell structure on the $(11\overline{2}1)$ plane and enrich with Zr, Y and Zn. A series of models with five-periodic-supercell structures are tried to analyze the atomic distribution of NSPs on different planes, including Model 1 (Random distribution of atoms), model 2 (Er, Y, and Zn atoms segregated in the (0001) plane), model 3 (Er, Y, and Zn atoms segregated in the $(11\overline{2}0)$ plane), as exhibited in Fig. 9. The model 4 gives the lowest formation energies of - 2.292 eV atom⁻¹, indicating that the NSPs have five-periodic-supercell structures with

Table 1 EDS results of the Mg₉₈Y₁Zn₁ and Mg_{97.5}Y₁Zn₁Er_{0.5} alloys from the positions, as shown in Fig. 2(e) and 2(f).

Element	at%			
	Mg	Y	Er	Zn
A	89.6	5	0	5.4
В	25.5	28.0	0	46.5
C	39.8	17.1	4.9	38.2
D	91.6	3.4	0.9	4.1

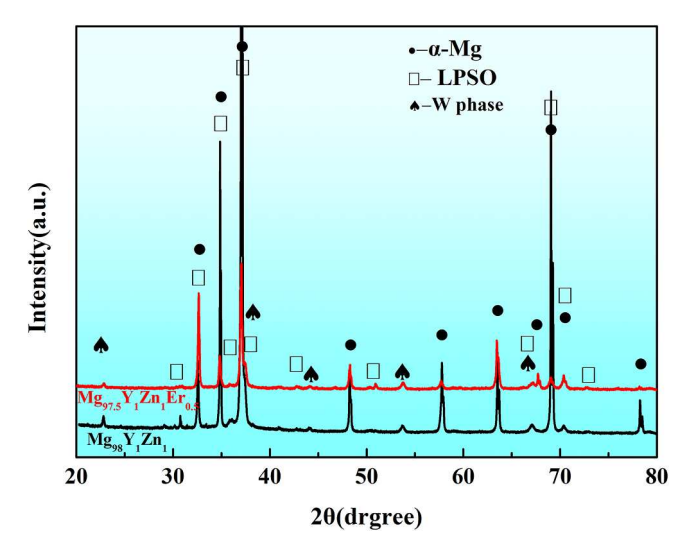


Fig. 3. XRD patterns of the cast $Mg_{98}Y_1Zn_1$ and $Mg_{97.5}Y_1Zn_1Er_{0.5}$ alloys.

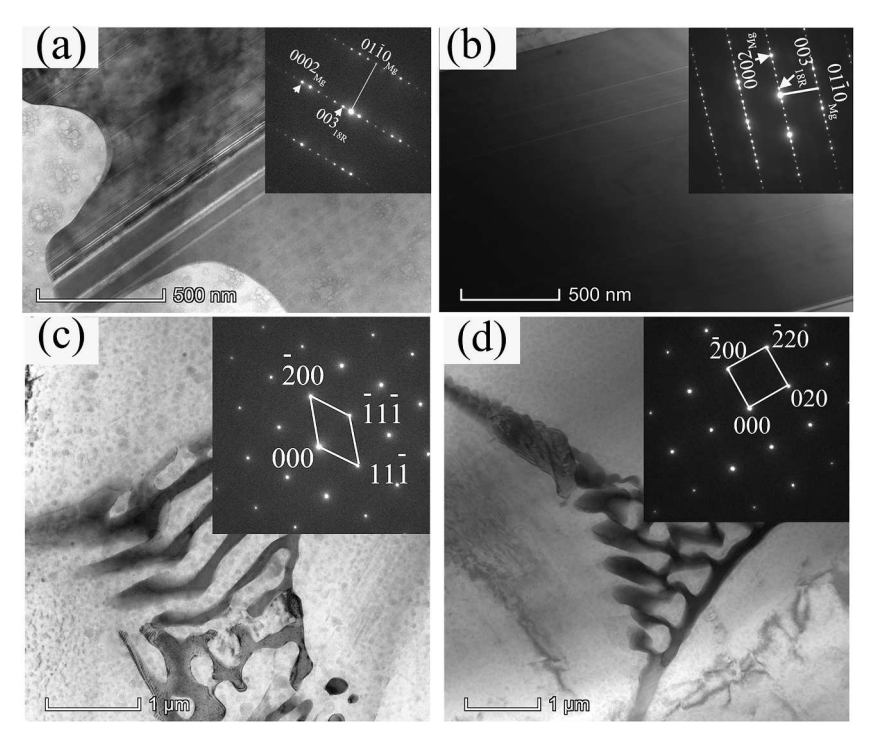


Fig. 4. TEM images and corresponding SAED patterns of the LPSO phase in (a) $Mg_{98}Y_1Zn_1$ and (b) $Mg_{97.5}Y_1Zn_1Er_{0.5}$ alloys. The TEM images and corresponding SAED patterns of the W phase in (c) $Mg_{98}Y_1Zn_1$ and (d) $Mg_{97.5}Y_1Zn_1Er_{0.5}$ alloys.

Er, Y, and Zn atoms segregated on the $(11\overline{2}1)$ plane.

4.2. Strengthening mechanisms

As a heavy rare earth element, Er has a large solid solubility in magnesium matrix (32.7 wt percent (wt.%)] at the eutectic temperature). The influence of Er on Mg alloys can be summarized as the following five aspects after reviewing literature: (1) Due to its large solid solubility of Er in magnesium matrix, it is difficult to form Mg-RE intermetallic phase (Rokhlin, 2003; Peng et al., 2008). However, sometimes Er along with Y can facilitate the formation of LPSO. For instance, in Mg-RE(Y/Er)-Zn alloys, LPSO phase and W phase can be formed (Feng et al., 2019). When (Y,Er)/Zn atomic ratio is \geq 1, LPSO phase can be mainly formed (Zhu et al., 2017). (2) Er can refines grains through grain boundary segregation (Jung et al., 2015). (3) Er can contribute strength through solid solution

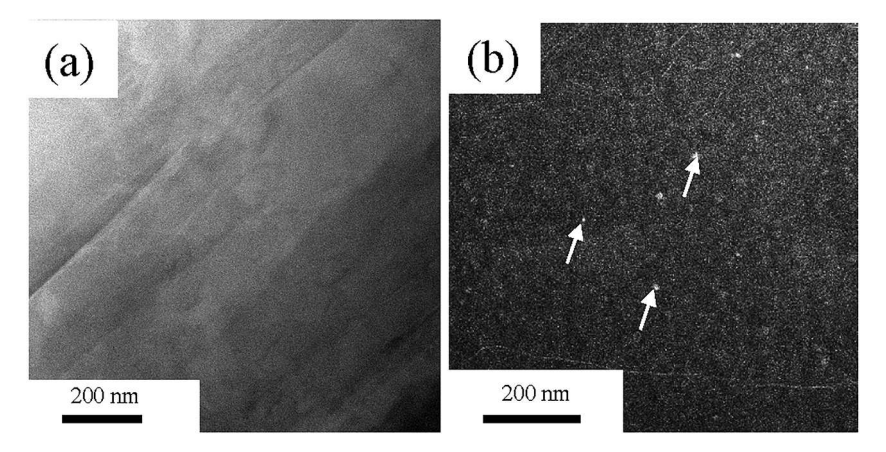


Fig. 5. HAADF-TEM images of as-cast (a) Mg₉₈Y₁Zn₁ and (b) Mg_{97.5}Y₁Zn₁Er_{0.5} alloys. The precipitates are marked by the white arrows. HAADF-TEM images of (a) and (b) are characterized by TEM, FEI Talos F200X G2 and TEM, FEI Themis Z with spherical aberration correctors, respectively.

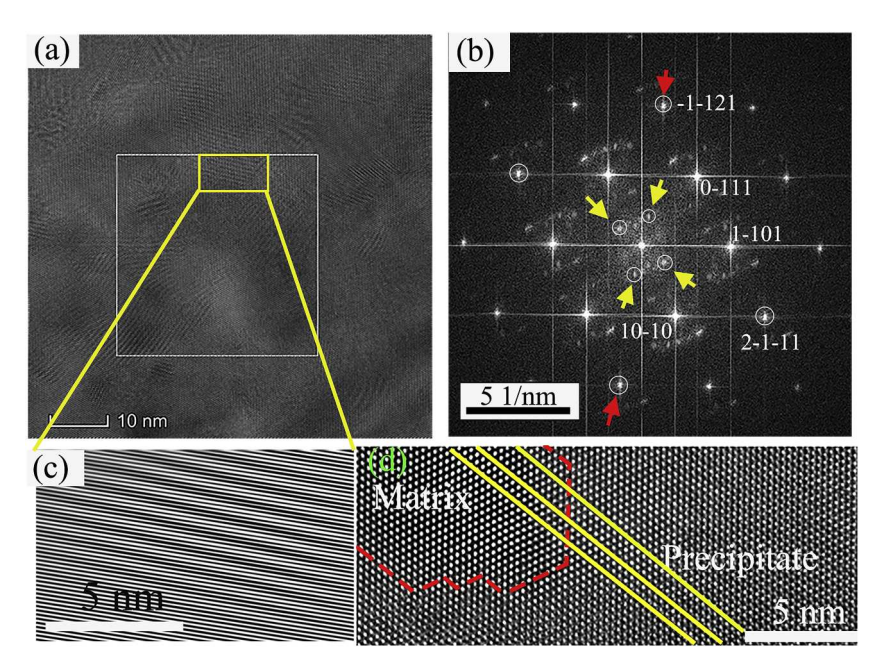


Fig. 6. (a) high-resolution TEM images of the cast $Mg_{97.5}Y_1Zn_1Er_{0.5}$ alloy, (b) the FFT patterns corresponding to a local region indicated by a white box in (a), (c) the IFFT images corresponding to (a), (d) the interface between a NSP and Mg matrix.

strengthening (Jung et al., 2015). (4) Er can reduce the stacking fault energy and promote the activation of < c + a >slip system, increasing the ductility of Mg alloys (Sandlöbes et al., 2014). In addition, it is also reported that Er can weaken the texture in the wrought Mg alloys (Jung et al., 2015; Robson et al., 2014).

As indicated above that the effective grain sizes, texture and the LPSO (structures, microhardness and the volume fractions) are not affected by the addition of Er. Hence, yield strength could not be improved by above factors. The addition of Er may contribute to the strength through solution strengthening (He et al., 2021; Zhang et al., 2021a). Thus, the solution strengthening is evaluated by (Fan et al., 2022),

$$\sigma_{\text{KS}} = CX^{2/3} \tag{4}$$

where C is the strengthening rate, and X is estimated as 0.2% from the EDS analysis in Table 2. Because of a lack of C for Er in magnesium in open literatures, C for Y [1249 MPa (at%) $^{-2/3}$] is used as C for Er due to their similar atomic sizes (Er: 1.76 Å, Y: 1.80 Å) (Gao et al., 2009). The solid-solution strengthening of the Er contribution can be evaluated approximately as 17 MPa for Mg97.5Y1Zn1Er0.5, which is far lower than the actual measured value (77 MPa) and plays an insignificant role in strengthening. Therefore, the NSPs play the most important role in increasing the yield strength of the Er-containing alloy.

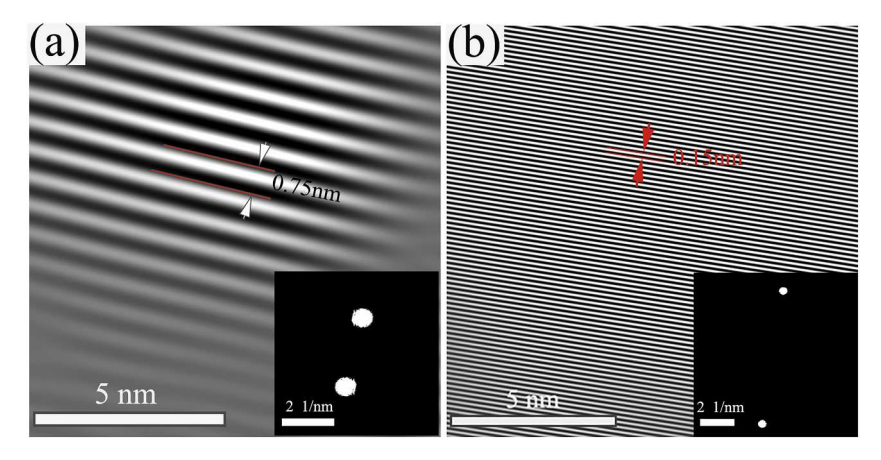


Fig. 7. The width of the superlattice (a) and Mg matrix (b) through IFFT images and selected zone diffraction patterns (inset) in the $Mg_{97.5}Y_1Z_1$ $n_1Er_{0.5}$ alloy.

Besides the contribution of solid-solution strengthening, the NSPs actually contribute 60 MPa through the test value. In general, the precipitation-strengthening mechanisms can be divided into two categories i.e., the dislocation-shearing mechanism (Chen et al., 2021) and the Orowan mechanism (Barnett et al., 2019) of dislocation bypassing. The Orowan equation is used to estimate the strengthening effect of the nanoscale precipitates (Nie, 2003):

$$\Delta\sigma_{Orowan} = \frac{MGb}{2\pi\sqrt{1-\nu}\left(0.825\sqrt{\frac{l_w}{f}} - 0.393l - 0.886w\right)} \times \ln\left(\frac{l}{b}\right)$$
 (5)

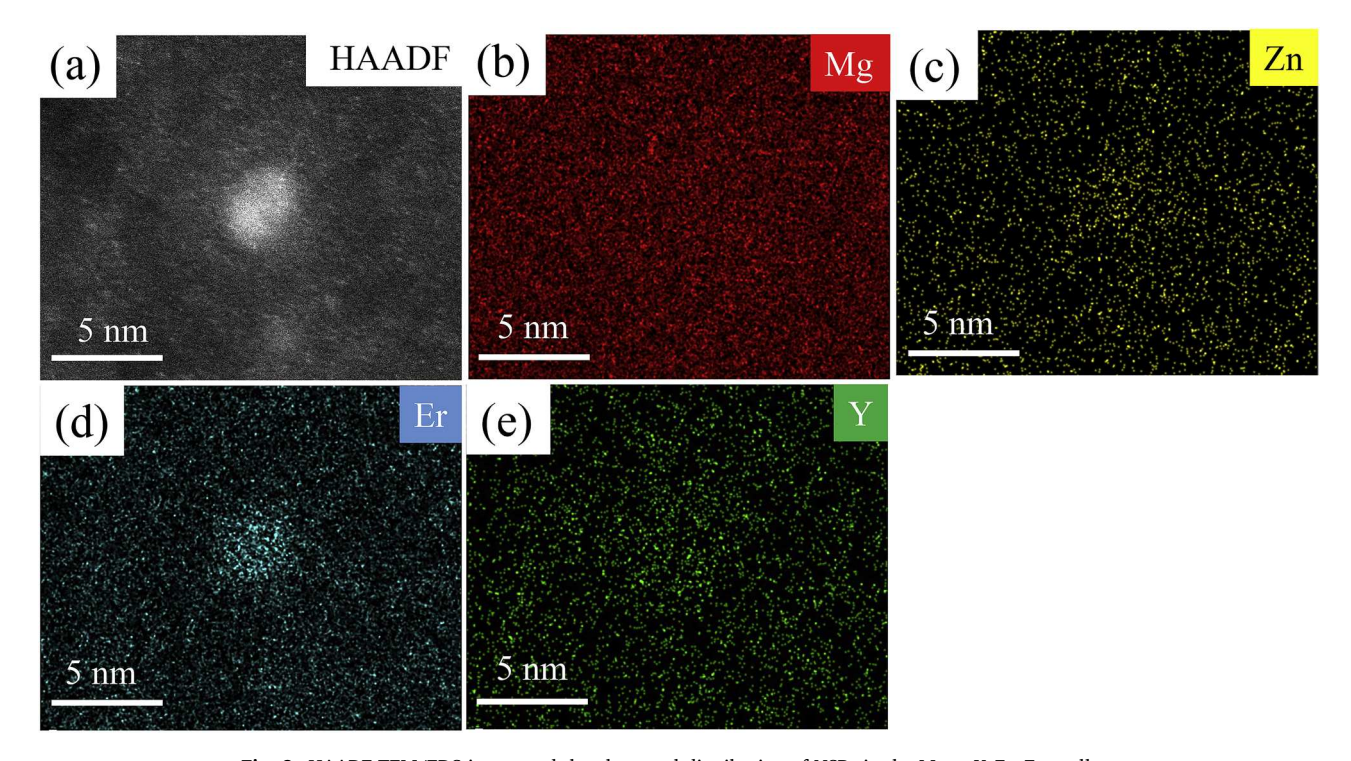
where M (4.5) is the Taylor factor (Cáceres and Lukáč, 2009), and G is the shear modulus of the Mg matrix (16.6 GPa) (Qiao et al., 2017). The I and W are the length and width of precipitates, and are estimated as 8 nm. V is the Poisson ratio of 0.32 for Mg (Zhang et al., 2019), f represents the volume fraction of the NSPs, which is estimated as 0.14% by Eq. (1). D (0.32 nm) represents the Burgers vector (Zhang et al., 2019). In this work, the main slip system in the alloy is basal D dislocation rather than D dislocation. This will be discussed in the next section. Thus, the Burgers vector 0.32 nm for basal D dislocation is used to estimate the strengthening effect. Through Eq. (5), the contribution from the Orowan strengthening by NSPs is estimated as 90 MPa, which is far higher than the actual measured value (60 MPa), suggesting that the Orowan mechanism is not the dominated mechanism for contributing to the strength. This result is consistent with the result that no dislocation loops were found around NSPs in the TEM observation (Fig. 10).

To identify the interaction between the NSPs and dislocations during deformation, the cast $Mg_{97.5}Y_1Zn_1Er_{0.5}$ alloy was strained with an 8% deformation. And then HAADF-TEM images and corresponding high-resolution TEM images of the NSPs in 8%-strained were observed, as shown in Fig. 10(a) and 10(b). Fig. 10(c) and 10(d) are the IFFT images of region 1 and region 2 shown in Fig. 10(b), respectively. It is found that there are dislocations in the regions corresponding to the two NSPs, suggesting that the NSPs are sheared by dislocations during deformation.

The dislocation-shearing mechanism is activated when the fine precipitates are coherent with the matrix (Ming et al., 2018; Wang et al., 2018). In the present work, the size and interface relationship of the NSPs satisfy the criteria, which provides favorable conditions for the dislocation-shearing mechanism. To identify the dislocation-shearing mechanism of the NSPs during deformation, the loading-unloading-reloading tests (unloading at strains: 2%, 4%, 6%, 8%) for alloys with and without NSPs were performed and the back-stress of the two alloys was evaluated according to the equation: $\sigma_{back\ stress} = (\sigma_r + \sigma_u) / 2$ (Yang et al., 2016), where σ_u is the unloading yield stress and σ_r is the reloading yield stress. The true stress-strain curves and the back-stress of Mg₉₈Y₁Zn₁ and Mg_{97.5}Y₁Zn₁Er_{0.5} alloys are shown in Fig. 11(a) and (b), respectively. By comparing the back-stress of alloys with and without NSPs, it can be concluded that NSPs contribute very few to the back stress during deformation. Maciejewski et al. indicated that when the precipitates are smaller than the critical size, it corresponds to the dislocation shear mechanism, and the back-stress generated by precipitates is very small (Maciejewski and Ghonem, 2014). The result of the similar back-stress in alloys with and without NSPs confirms again the shearing mechanism of the NSPs.

The increment in the yield strength through shearing mechanisms of NSPs can mainly be contributed by coherent strengthening ($\Delta\sigma_{CS}$), modulus strengthening ($\Delta\sigma_{MS}$), and order strengthening ($\Delta\sigma_{OS}$) (Liu et al., 2022). In general, the larger one of $\Delta\sigma_{MS} + \Delta\sigma_{CS}$ and $\Delta\sigma_{OS}$ determines the resultant contribution in these sequential processes (Liu et al., 2022). The formulas that can be used to calculate the strength increment caused by the shearing mechanism are as follows (Xu et al., 2019):

$$\Delta\sigma_{CS} = M \cdot \alpha_{\varepsilon} (G \cdot \varepsilon_c)^{3/2} \left(\frac{rf}{0.5Gb}\right)^{1/2}$$
(6)



9

 $\textbf{Fig. 8.} \ \ \text{HAADF-TEM/EDS image and the elemental distribution of NSPs in the } Mg_{97.5}Y_1Zn_1Er_{0.5} \ alloy.$

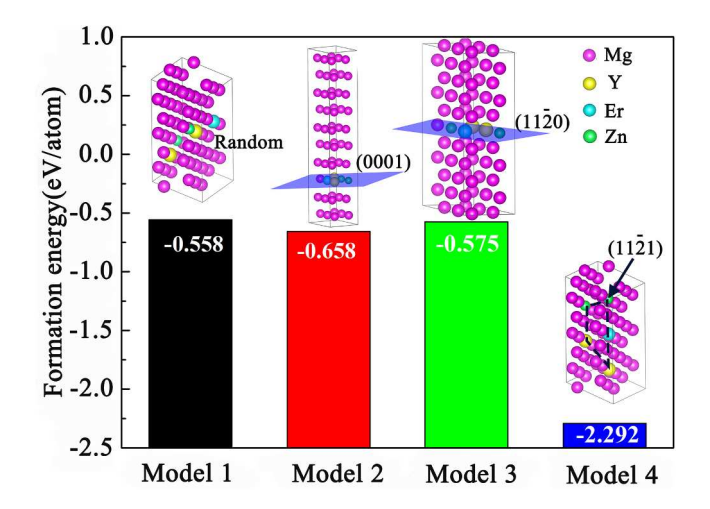


Fig. 9. DFT calculations of formation energies of NSPs with different sublattice occupancies of Er, Y and Zn.

 $\label{eq:continuous} \textbf{Table 2} \\ \text{EDS results of the Mg matrix in } Mg_{97.5}Y_1Zn_1Er_{0.5} \text{ alloys.}$

Element	Mg	Y	Er	Zn
Mg matrix(at%)	98.5	0.6	0.2	0.7

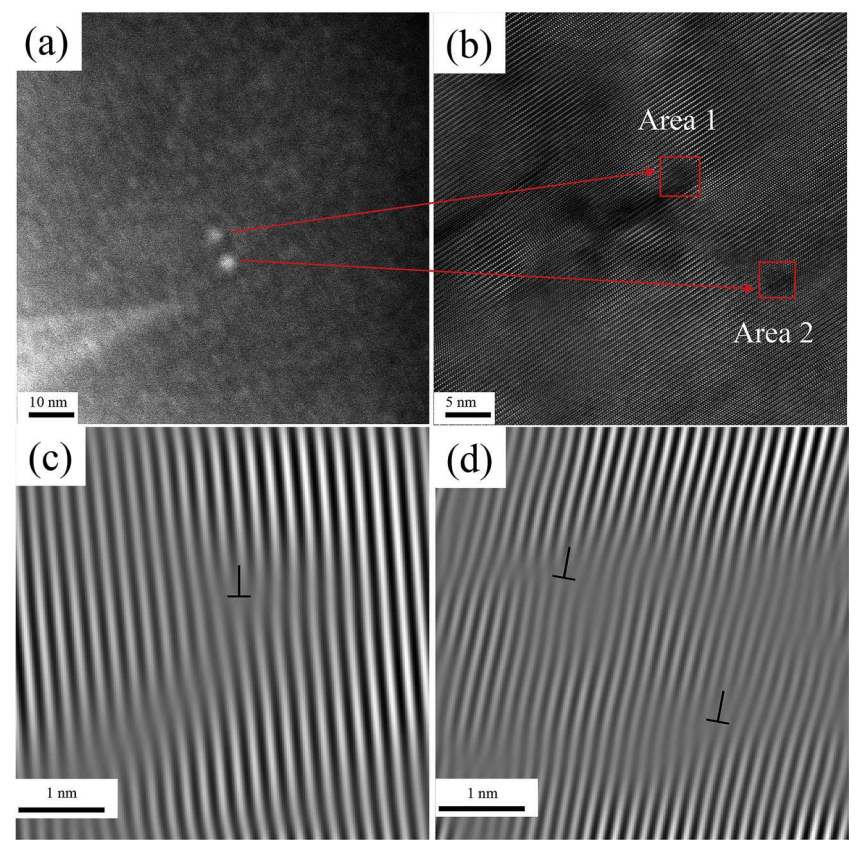


Fig. 10. The interaction between dislocations and NSPs. (a) HAADF-TEM images of NSPs in 8%-strained $Mg_{97.5}Y_1Zn_1Er_{0.5}$ alloy, (b) high-resolution image corresponding to the NSPs in (a), (c) and (d) the IFFT images of area 1 and area 2 in Fig.(b), respectively, indicating the shearing of NSPs by dislocations.

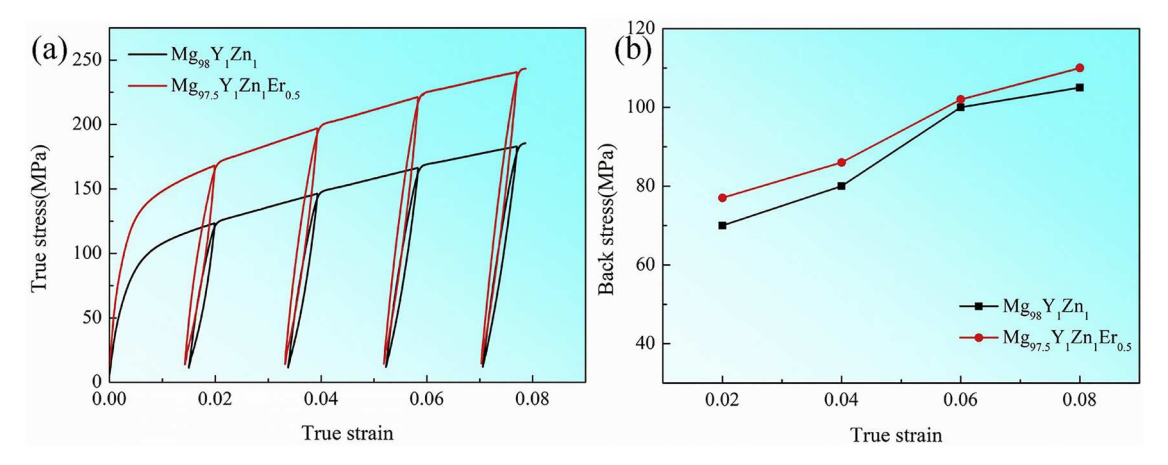


Fig. 11. (a) Loading-unloading-reloading (LUR) true stress-strain curves of the two alloys, (b) back-stress at various true strains.

$$\Delta \sigma_{MS} = M \times 0.0055 (\Delta G)^{3/2} \times \left(\frac{2f}{G}\right)^{\frac{1}{2}} \times \left(\frac{r}{b}\right)^{\frac{3m}{2}-1} \tag{7}$$

$$\Delta\sigma_{OS} = M \cdot 0.81 \frac{\gamma_{APB}}{2b} \left(\frac{3\pi f}{8}\right)^{1/2} \tag{8}$$

where M is the Taylor factor (4.5) (Cáceres and Lukáč, 2009), G is the shear modulus (16.6 GPa), ε_c is the constrained lattice-parameter mismatch (2 η /3), f represents the volume fraction of the NSPs (0.14%), b (0.32 nm) represents the Burgers vector (Zhang et al., 2019), r is the average radius of NSPs (4 nm), γ_{APB} is the average anti-phase boundary energy, m is 0.85 (Zhao et al., 2017), and ΔG is the shear-modulus mismatch between the NSPs and Mg matrix.

Based on Eq. (6), the $\Delta\sigma_{CS}$ is calculated as 0.6 MPa, indicating that the $\Delta\sigma_{CS}$ is a weak effect in strengthening and is negligible. From Eqs. (7) and (8), it is considered that the cause of deviation is closely related to ΔG and γ_{APB} . The relationship between $\Delta\sigma_{MS}$ and $\Delta\sigma_{OS}$ is the competition rather than superposition. Therefore, the ΔG and γ_{APB} are discussed separately.

Firstly, if the strength increment (60 MPa) is from modulus strengthening, the ΔG should be 20.5 GPa, and the shear modulus of the NSPs needs to reach 37.1 GPa. However, ab initio density functional theory calculations of the elastic properties of Mg-RE intermetallic compounds show that most of the components of the single-crystal stiffness tensors are similar to those of Mg (Ji et al., 2014). Moreover, the dislocations may not be able to shear the precipitates with such a high shear modulus. Therefore, the modulus strengthening can not be the dominated mechanism for contributing to the strength. Next, whether $\Delta \sigma_{OS}$ is the main strengthening mechanism is verified.

Similarly, if the strength increment (60 MPa) is contributed by order strengthening, the γ_{APB} can be calculated from the experimental value as 0.25 J/m². This value is close to the reported average anti-phase boundary energy of Mg₃RE precipitates (an HCP structure) in Mg alloys (0.18 J/m²) (Guo et al., 2021; Issa et al., 2014). Therefore, the γ_{APB} is reasonable since the NSP contains the same HCP structure, indicating that the order strengthening of NSPs plays the most important role. The NSPs possess a higher anti-phase boundary energy as compared with other RE-containing precipitates, such as Mg₃RE precipitates, which leads to greater ordered strengthening.

4.3. Ductile mechanisms

In the present work, although NSPs are introduced into the Mg-Y-Zn alloy to increase the yield and tensile strength significantly, the tensile ductility of the alloy is not sacrificed and retained as the same as that of the Mg-Y-Zn alloy without NSPs. It is found that the elongation of both alloys mainly depends on the uniform elongation (Mg₉₈Y₁Zn₁: 12% and Mg_{97.5}Y₁Zn₁Er_{0.5} alloys:13%), as shown in the Fig. 12(a). The uniform elongation close to total elongation (Mg₉₈Y₁Zn₁: 13% and Mg_{97.5}Y₁Zn₁Er_{0.5} alloys:13%). Therefore, only the uniform elongation is discussed. The fracture surfaces show that there are uniformly distributed dimples in the two alloys, as shown in Fig. 12(b) and (c), showing that the cracks are uniformly generated in matrix during the fracture process of the Mg₉₈Y₁Zn₁ and Mg_{97.5}Y₁Zn₁Er_{0.5} alloys.

Based on Considère criterion (Fu et al., 2020), the work-hardening rate ($d\sigma/d\epsilon$) (Murr, 2015) is the main parameter that influences the uniform deformation of the coarse-grained material. The work hardening can be related to twins and/or dislocations. The EBSD analysis of twins are shown in Fig. 13(a) and 13(b). The { $10\overline{1}2$ } extension twin and { $10\overline{1}1$ } contraction twin are most commonly twinning models (Habib et al., 2017; Xie et al., 2022). Obviously, the boundaries with a misorientation of $<1\overline{2}10>86.3$ °correspond to { $10\overline{1}2$ } extension twin, and the boundaries with a misorientation of $<1\overline{2}10>56$ ° correspond to { $10\overline{1}1$ } contraction twin (Jin et al., 2010; Zhang et al., 2017b). It is found that the twins in this work are { $10\overline{1}2$ } extension twins rather than { $10\overline{1}1$ } contraction twins

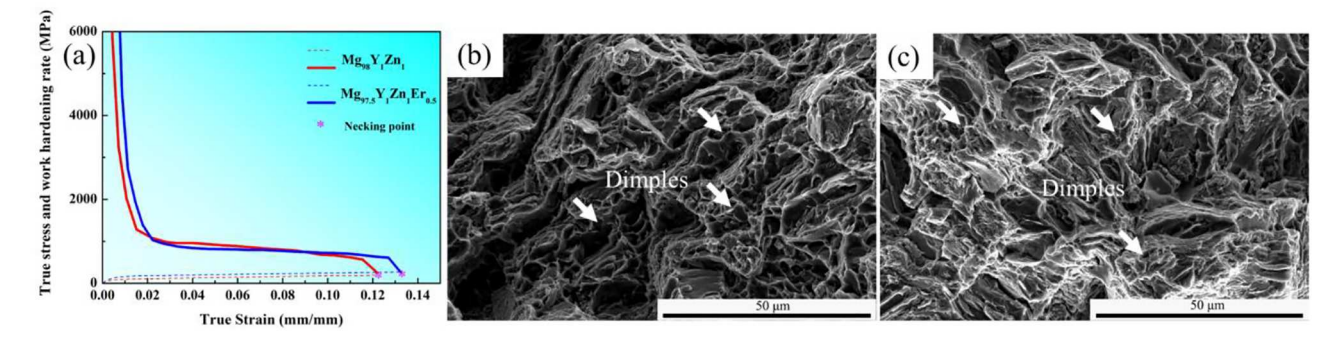


Fig. 12. (a)The true stress-strain curves and the work-hardening $(d\sigma/d\epsilon)$ curves of the tensile specimens for the Mg₉₈Y₁Zn₁ alloy and Mg_{97.5}Y₁Zn₁Er_{0.5} alloy; (b) and (c) the fracture morphologies of the Mg₉₈Y₁Zn₁ alloy and Mg_{97.5}Y₁Zn₁Er_{0.5} alloy, respectively.

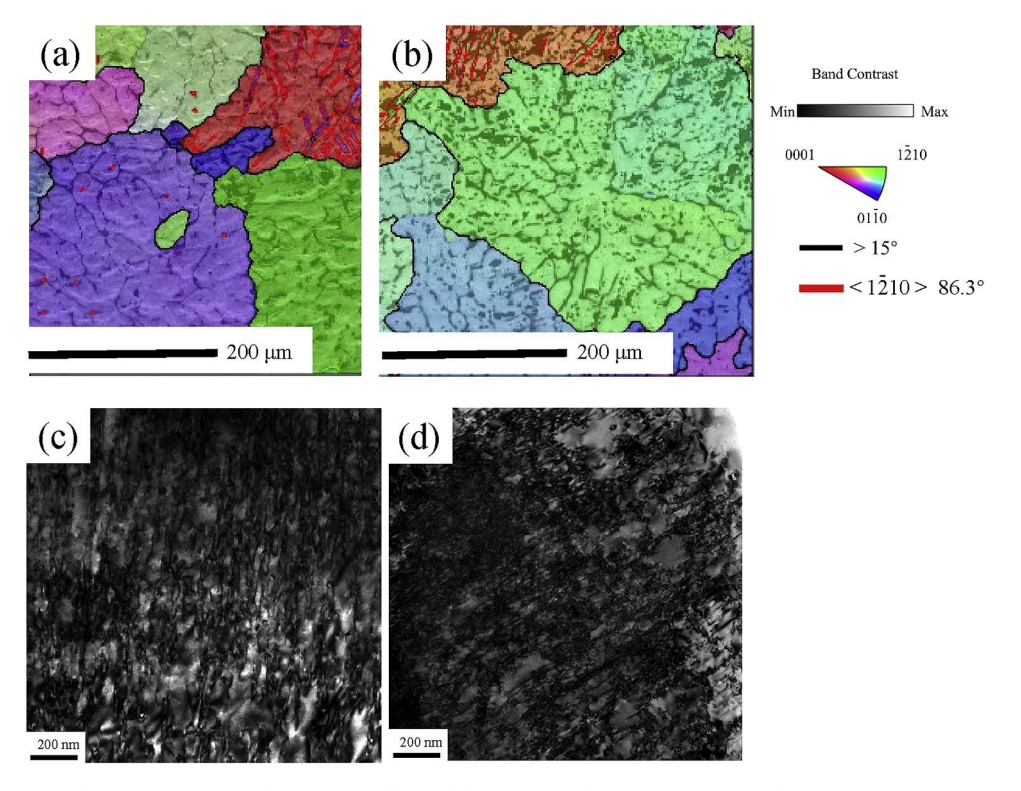


Fig. 13. The EBSD analysis of (a) 8%-strained $Mg_{98}Y_1Zn_1$ alloy and (b) 8%-strained $Mg_{97.5}Y_1Zn_1Er_{0.5}$. Dislocation configurations of 8%-strained (c) $Mg_{98}Y_1Zn_1$ and (d) $Mg_{97.5}Y_1Zn_1Er_{0.5}$ alloys. The zone axis is $[2\overline{11}0]$.

(Fig. 13). Most important, a small amount of twinning is present in both alloys strained at 8%. Therefore, twinning behavior is not affected by the addition of Er. Table 3 list the dislocation densities in the as-cast and 8%-strained samples. It is clear that the dislocation density is almost the same for the cast Mg₉₈Y₁Zn₁ and cast Mg_{97.5}Y₁Zn₁Er_{0.5}, indicating that the dislocation density is not affected by the introduction of NSPs at the cast state. However, upon straining, the dislocation density in 8%-strained Mg_{97.5}Y₁Zn₁Er_{0.5} is much higher than in 8%-strained Mg₉₈Y₁Zn₁, indicating that NSPs enhance the multiplication of dislocations during deformation. This is in agreement with some previous results that dislocations can multiplication when dislocation shear precipitates in alloys (Feng et al., 2021). Moreover, the multiplication of dislocations consists of $\langle a \rangle$ and $\langle c + a \rangle$ dislocations, as shown in Fig. 13(c) and 13(d). Additional amount of the dislocation density (\sim 0.8 \times 10¹⁵ m^{-2}) is introduced due to the activation of $\langle c + a \rangle$ dislocations. In general, precipitation strengthening always leads to a low work hardening rate since the dislocation pinning of particles contributes to only the yield strength (Wei et al., 2022; Xu et al., 2020, 2019). A significant increase in yield strength induced by precipitation hardening can lead to a very high yield ratio, the yield strength can even be equivalent to tensile strength without dislocation multiplication (He et al., 2017; Li et al., 2022). However, it is clear from Fig. 12(a) that both cast alloys with and without NSPs have almost the same work-hardening rate during deformation though NSPs enhance the yield strength significantly in Mg_{97.5}Y₁Zn₁Er_{0.5}. This can be explained well by the dislocation multiplication induced by NSPs during deformation.

The ductility of Mg alloys with HCP structure is strongly dependent on the activation of various dislocation slip systems (Habib et al., 2019). The active slip systems in 8%-strained Mg₉₈Y₁Zn₁ and Mg_{97.5}Y₁Zn₁Er_{0.5} alloys were identified through TEM observations under double-beam conditions. According to the invisibility criterion of $g \cdot b = 0$, where g and b represent the reflection and Burgers vector, respectively. If a particular reflection vector is set as g = 0002, $\langle c \rangle$ dislocations and $\langle c + a \rangle$ dislocations are visible, while $\langle a \rangle$ dislocations are invisible. In contrast, when the reflection vector is set as $g = 01\overline{10}$, the $\langle a \rangle$ and $\langle c + a \rangle$ dislocations become visible, while $\langle c \rangle$ dislocations are invisible (Wei et al., 2021). Thus, the type of dislocations can be identified by comparative analyzing of images in the same region obtained under different two-beam conditions. For the 8%-strained Mg₉₈Y₁Zn₁ alloy, the TEM image using double-beam conditions are shown in Fig. 14. Dislocations are invisible with the reflection vector of g = 0002, as shown in Fig. 14(a), 14(b) and 14(c), indicating that there are no $\langle c \rangle$ and $\langle c + a \rangle$ dislocations in the 8%-strained Mg₉₈Y₁Zn₁ alloy. Dislocations are visible

Table 3 The dislocation densities ($\times 10^{15} \text{ m}^{-2}$) of the as-cast and 8%-strained samples in Mg₉₈Y₁Zn₁ and Mg_{97.5}Y₁Zn₁Er_{0.5} alloys.

		• • • • • • • • • • • • • • • • • • • •	•
	$Mg_{98}Y_1Zn_1$		$Mg_{97.5}Y_1Zn_1Er_{0.5}$
As-cast samples	0.29		0.3
8%-strain samples	2.2		3
Increment	1.9		2.7

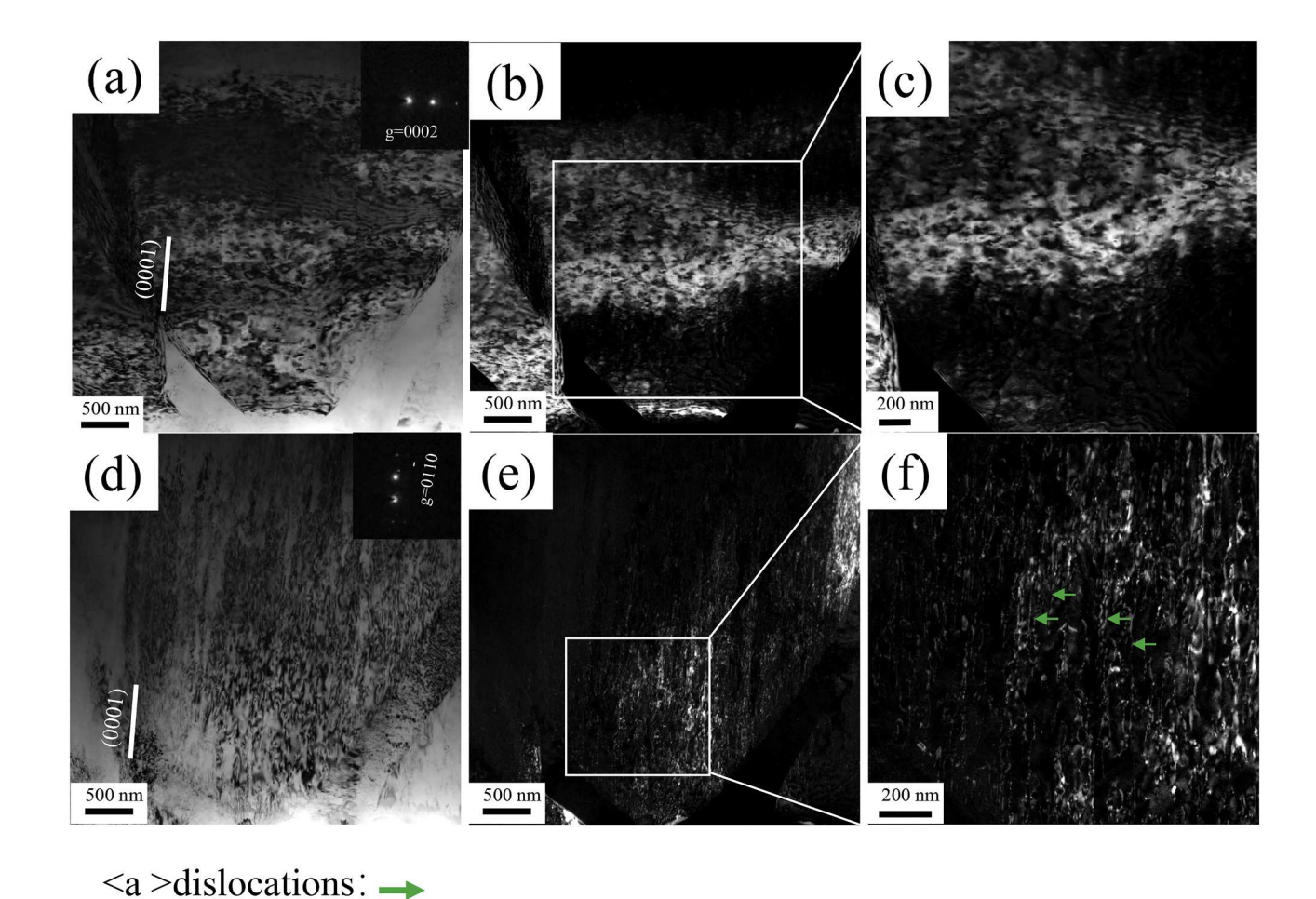


Fig. 14. Dislocation configurations in the 8%-strained $Mg_{98}Y_1Zn_1$ alloy. (a) TEM bright-field images viewed with g=0002, (b) TEM dark-field images viewed with g=0002, (c) local magnified image from (b); (d) TEM bright-field images viewed with $g=01\overline{1}0$, (e) TEM dark-field images viewed with $g=01\overline{1}0$, (f) local magnified image from (e). (a), (b), (d) and (e) are taken from the same region. The zone axis is $[2\overline{11}0]$. Green arrows indicate the $\langle a \rangle$ dislocations.

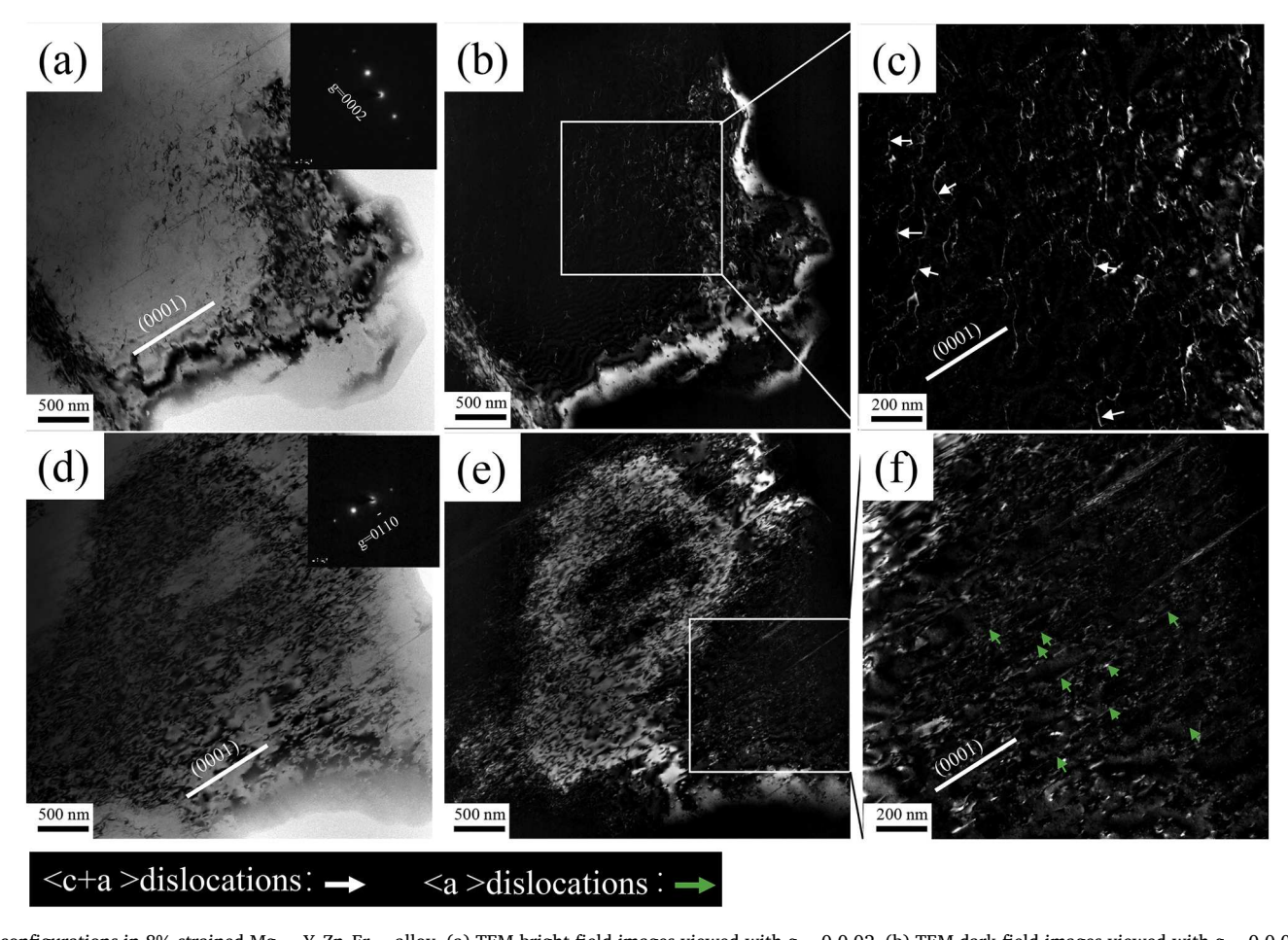


Fig. 15. Dislocation configurations in 8%-strained Mg_{97.5}Y₁Zn₁Er_{0.5} alloy. (a) TEM bright-field images viewed with g=0 0 02, (b) TEM dark-field images viewed with g=0 0 02, (c) local magnified image from (b); (d) TEM bright-field images viewed with g=0 1 0 02, (c) local magnified image from (e). (a), (b), (d) and (e) are taken from the same region. The zone axis is $[2\overline{11}0]$. Green arrows indicate the $\langle a \rangle$ dislocations, while white arrows indicate the $\langle c+a \rangle$ dislocations.

with the reflection vector of $g = 01\overline{10}$, as shown in Fig. 14(d), 14(e) and 14(f), indicating that only basal $\langle a \rangle$ dislocations, marked by the green arrows, are formed in the deformed Mg₉₈Y₁Zn₁ sample. This is consistent with the well-known theory that base-slip system is more easily activated in HCP metals because of their low critical resolved shear stress (CRSS) (Stanford et al., 2008; Xie et al., 2021).

For the 8%-strained Mg_{97.5}Y₁Zn₁Er_{0.5} alloy, the TEM images under double-beam conditions are shown in Fig. 15. Some dislocations are visible with the reflection vector of g=0002, as marked by the white arrows in Fig. 15(c), indicating the existence of $\langle c+a\rangle$ dislocations. When the reflection vector is changed to $g=01\overline{10}$, some dislocations are visible, as marked by the green arrows in Fig. 15 (f), corresponding to $\langle a \rangle$ dislocations. These results indicate that the slip dislocations are mostly basal $\langle a \rangle$ dislocations and a few $\langle c+a \rangle$ dislocations are multiplicated during deformation. Thus, it is basal $\langle a \rangle$ dislocation rather than $\langle c+a \rangle$ dislocation that is the main slip system contributing to the yield strength. However, during deformation, the 8% Mg_{97.5}Y₁Zn₁Er_{0.5} alloy activates the $\langle c+a \rangle$ dislocations slip systems, contributing to the ductility due to the introduction of NSPs.

5. Conclusions

A new cast Mg-Y-Zn-Er alloy with a comprehensive strength-ductility synergy is developed by introducing the NSPs through rareearth Er alloying. The formation of NSPs and their strengthening/ plasticizing are investigated systematically. The following conclusions can be drawn:

- 1 The cast $Mg_{98}Y_1Zn_1$ alloy has a yield strength of 77 MPa with an elongation of 13%. The introduction of the NSPs into cast $Mg_{98}Y_1Zn_1$ alloy double the yield strength without scarifying the ductility. The cast $Mg_{97.5}Y_1Zn_1Er_{0.5}$ alloy strengthened by NSPs has a yield strength of 154 MPa, a tensile strength of 234 MPa, and an elongation of 13%.
- 2 The addition of Er in the Mg-Y-Zn alloy does not change the microstructures, including the effective grain size, the reticular-distributed 18R LPSO phase, and W phase. However, the precipitation of NSPs is promoted due to the addition of Er.
- 3 The formation of the NSPs in $Mg_{97.5}Y_1Zn_1Er_{0.5}$ alloys is promoted by the segregation of Er, Y, and Zn atoms in the $(11\overline{2}1)$ plane due to the lower formation energy. The NSPs with a radius of around 4 nm have a five-periodic-supercell structure and are coherent with the Mg matrix.
- 4 The fine NSPs distribute in the Mg matrix uniformly. The excellent strength is contributed mainly by the ordering strengthening of the NSPs through the dislocation-shearing mechanism and solid-solution strengthening.
- 5 The dislocation density in strained $Mg_{97.5}Y_1Zn_1Er_{0.5}$ is much higher than in strained $Mg_{98}Y_1Zn_1$. Both $\langle c+a\rangle$ and $\langle a\rangle$ dislocations can be activated in $Mg_{97.5}Y_1Zn_1Er_{0.5}$ alloy while only $\langle a\rangle$ dislocations can be activated in $Mg_{98}Y_1Zn_1$ alloy. NSPs enhance the multiplication of dislocations during deformation. Both dislocation multiplication and the activation of $\langle c+a\rangle$ dislocation system contribute to the ductility at a high yield strength level.

CRediT authorship contribution statement

Mingyu Fan: Conceptualization, Methodology, Validation, Formal analysis, Investigation, Writing – original draft, Visualization. Zhongwu Zhang: Conceptualization, Methodology, Supervision, Resources, Writing – review & editing, Formal analysis. Ye Cui: Conceptualization, Methodology, Writing – original draft, Resources, Formal analysis. Liyuan Liu: Investigation, Formal analysis. Yingwei Liu: Formal analysis. Peter K. Liaw: Supervision, Conceptualization, Writing – review & editing.

Declaration of Competing Interest

The authors declare that they have no known competing financial interests or personal relationships that could have appeared to influence the work reported in this paper.

Data availability

No data was used for the research described in the article.

Acknowledgments

The present work was supported by the NSFC Funding (U2141207, 52001083, 51701051 and 52171111) and Heilongjiang Touyan Innovation Team Program. PKL very much appreciates the supports from the National Science Foundation (DMR-1611180 and 1809640).

References

Agnew, S.R., Nie, J.F., 2010. Preface to the viewpoint set on: the current state of magnesium alloy science and technology. Scr. Mater. 63, 671–673.

Agnew, S.R., Singh, A., Calhoun, C.A., Mulay, R.P., Bhattacharyya, J.J., Somekawa, H., Mukai, T., Clausen, B., Wu, P.D., 2018. In-situ neutron diffraction of a quasicrystal-containing Mg alloy interpreted using a new polycrystal plasticity model of hardening due to {10.2} tensile twinning. Int. J. Plast. 100, 34–51.

Barnett, M.R., Wang, H., Guo, T., 2019. An Orowan precipitate strengthening equation for mechanical twinning in Mg. Int. J. Plast. 112, 108–122.

- Cáceres, C.H., Lukáč, P., 2009. Strain hardening behaviour and the Taylor factor of pure magnesium. Philo. Mag. 88, 977-989.
- Chen, H., Chen, Z., Ji, G., Zhong, S., Wang, H., Borbély, A., Ke, Y., Bréchet, Y., 2021. The influence of shearable and nonshearable precipitates on the Portevin-Le Chatelier behavior in precipitation hardening AlMgScZr alloys. Int. J. Plast. 147, 103120.
- Cheng, P., Zhao, Y., Lu, R., Hou, H., 2018. Effect of the morphology of long-period stacking ordered phase on mechanical properties and corrosion behavior of cast Mg-Zn-Y-Ti alloy. J. Alloys Compd. 764, 226–238.
- Fan, M., Cui, Y., Zhang, Y., Wei, X., Cao, X., Liaw, P.K., Yang, Y., Zhang, Z., 2022. Achieving high strength-ductility synergy in a Mg97Y1Zn1Ho1 alloy via a nano-spaced long-period stacking-ordered phase. J. Magnes. Alloy. DOI https://doi.org/10.1016/j.jma.2022.01.002.
- Feng, L., Mills, M.J., Wang, Y., 2021. Generalized stacking fault energy surface mismatch and dislocation transformation. NPJ Comput. Mater. 7, 201.
- Feng, Y., Zhang, J., Qin, P., Liu, S., Yang, Q., Meng, J., Wu, R., Xie, J., 2019. Characterization of elevated-temperature high strength and decent thermal conductivity extruded Mg-Er-Y-Zn alloy containing nano-spaced stacking faults. Mater. Charact. 155, 109823.
- Fu, W., Huang, Y., Sun, J., Ngan, A.H.W., 2022. Strengthening CrFeCoNiMn0.75Cu0.25 high entropy alloy via laser shock peening. Int. J. Plast. 154, 103296.
- Fu, W., Zheng, W., Huang, Y., Guo, F., Jiang, S., Xue, P., Ren, Y., Fan, H., Ning, Z., Sun, J., 2020. Cryogenic mechanical behaviors of CrMnFeCoNi high-entropy alloy. Mater. Sci. Eng. A 789, 139579.
- Gao, L., Chen, R.S., Han, E.H., 2009. Effects of rare-earth elements Gd and Y on the solid solution strengthening of Mg alloys. J. Alloys Compd. 481, 379-384.
- Guo, Y., Liu, B., Xie, W., Luo, Q., Li, Q., 2021. Anti-phase boundary energy of β series precipitates in Mg-Y-Nd system. Scr. Mater. 193, 127–131.
- Guo, Y., Luo, Q., Liu, B., Li, Q., 2020. Elastic properties of long-period stacking ordered phases in Mg–Zn–Y and Mg–Ni–Y alloys: a first-principles study. Scr. Mater. 178, 422–427.
- Habib, S.A., Khan, A.S., Gnäupel-Herold, T., Lloyd, J.T., Schoenfeld, S.E., 2017. Anisotropy, tension-compression asymmetry and texture evolution of a rare-earth-containing magnesium alloy sheet, ZEK100, at different strain rates and temperatures: experiments and modeling. Int. J. Plast. 95, 163–190.
- Habib, S.A., Lloyd, J.T., Meredith, C.S., Khan, A.S., Schoenfeld, S.E., 2019. Fracture of an anisotropic rare-earth-containing magnesium alloy (ZEK100) at different stress states and strain rates: experiments and modeling. Int. J. Plast. 122, 285–318.
- He, B.B., Hu, B., Yen, H.W., Cheng, G.J., Wang, Z.K., Luo, H.W., Huang, M.X., 2017. High dislocation density-induced large ductility in deformed and partitioned steels. Science 357, 1029.
- He, Q.F., Tang, P.H., Chen, H.A., Lan, S., Wang, J.G., Luan, J.H., Du, M., Liu, Y., Liu, C.T., Pao, C.W., Yang, Y., 2021. Understanding chemical short-range ordering/demixing coupled with lattice distortion in solid solution high entropy alloys. Acta Mater. 216, 117140.
- He, S., 2007. Study on the Microstructural Evolution, Properties and Fracture Behavior of Mg-Gd-Y-Zr (-Ca) Alloys. Shanghai Jiao Tong University, Shanghai
- Issa, A., Saal, J.E., Wolverton, C., 2014. Physical factors controlling the observed high-strength precipitate morphology in Mg-rare earth alloys. Acta Mater. 65, 240–250.
- Ji, Y.Z., Issa, A., Heo, T.W., Saal, J.E., Wolverton, C., Chen, L.Q., 2014. Predicting β' precipitate morphology and evolution in Mg–RE alloys using a combination of first-principles calculations and phase-field modeling. Acta Mater. 76, 259–271.
- Jiang, S., Wang, H., Wu, Y., Liu, X., Chen, H., Yao, M., Gault, B., Ponge, D., Raabe, D., Hirata, A., Chen, M., Wang, Y., Lu, Z., 2017. Ultrastrong steel via minimal lattice misfit and high-density nanoprecipitation. Nature 544, 460–464.
- Jin, L., Dong, J., Wang, R., Peng, L.M., 2010. Effects of hot rolling processing on microstructures and mechanical properties of Mg–3%Al–1%Zn alloy sheet. Mater. Sci. Eng. A 527, 1970–1974.
- Jin, Z.-Z., Zha, M., Jia, H.-.L., Ma, P.-.K., Wang, S.-.Q., Liang, J.-.W., Wang, H.-.Y., 2021. Balancing the strength and ductility of Mg-6Zn-0.2Ca alloy via sub-rapid solidification combined with hard-plate rolling. J. Mate. Sci. Technol. 81, 219–228.
- Jin, Z.-.Z., Zha, M., Wang, S.-.Q., Wang, S.-.C., Wang, C., Jia, H.-.L., Wang, H.-.Y., 2022. Alloying design and microstructural control strategies towards developing Mg alloys with enhanced ductility. J. Magnes. Alloy 10, 1191–1206.
- Jung, I.-H., Sanjari, M., Kim, J., Yue, S., 2015. Role of RE in the deformation and recrystallization of Mg alloy and a new alloy design concept for Mg–RE alloys. Scr. Mater. 102, 1–6.
- Kawamura, Y., Kasahara, T., Izumi, S., Yamasaki, M., 2006. Elevated temperature Mg97Y2Cu1 alloy with long period ordered structure. Scr. Mater. 55, 453–456. Kim, J.-.K., Sandlöbes, S., Raabe, D., 2015. On the room temperature deformation mechanisms of a Mg–Y–Zn alloy with long-period-stacking-ordered structures. Acta Mater. 82, 414–423.
- Kishida, K., Nagai, K., Matsumoto, A., Yasuhara, A., Inui, H., 2015. Crystal structures of highly-ordered long-period stacking-ordered phases with 18R, 14H and 10H-type stacking sequences in the Mg–Zn–Y system. Acta Mater. 99, 228–239.
- Li, J., Chen, R., Ma, Y., Ke, W., 2013. Effect of Zr modification on solidification behavior and mechanical properties of Mg-Y-RE (WE54) alloy. J. Magnes. Alloy 1, 346–351.
- Li, K., Zhan, J., Yang, T., To, A.C., Tan, S., Tang, Q., Cao, H., Murr, L.E., 2022. Homogenization timing effect on microstructure and precipitation strengthening of 17–4PH stainless steel fabricated by laser powder bed fusion. Addit. Manuf. 52, 102672.
- Liao, H., Kim, J., Lee, T., Song, J., Peng, J., Jiang, B., Pan, F., 2020. Effect of heat treatment on LPSO morphology and mechanical properties of Mg–Zn–Y–Gd alloys. J. Magnes. Alloy 8, 1120–1127.
- Liu, L., Zhang, Y., Li, J., Fan, M., Wang, X., Wu, G., Yang, Z., Luan, J., Jiao, Z., Liu, C.T., Liaw, P.K., Zhang, Z., 2022. Enhanced strength-ductility synergy via novel bifunctional nano-precipitates in a high-entropy alloy. Int. J. Plast. 153, 103235.
- Lu, R., Wang, J., Chen, Y., Qin, D., Yang, W., Wu, Z., 2015. Effects of heat treatment on the morphology of long-period stacking ordered phase, the corresponding damping capacities and mechanical properties of Mg-Zn-Y alloys. J. Alloys Compd. 639, 541–546.
- Luo, K., Zhang, L., Wu, G., Liu, W., Ding, W., 2019. Effect of Y and Gd content on the microstructure and mechanical properties of Mg-Y-RE alloys. J. Magnes. Alloy 7, 345–354.
- Lyu, J., Kim, J., Liao, H., She, J., Song, J., Peng, J., Pan, F., Jiang, B., 2020. Effect of substitution of Zn with Ni on microstructure evolution and mechanical properties of LPSO dominant Mg-Y-Zn alloys. Mater. Sci. Eng. A 773, 138735.
- Maciejewski, K., Ghonem, H., 2014. Isotropic and kinematic hardening as functions of gamma prime precipitates in a nickel-based superalloy. Int. J. Fatigue 68, 123–135.
- Mayama, T., Agnew, S.R., Hagihara, K., Kamura, K., Shiraishi, K., Yamasaki, M., Kawamura, Y., 2022. α-Mg/LPSO (Long-Period Stacking Ordered) phase interfaces as obstacles against dislocation slip in as-cast Mg-Zn-Y alloys. Int. J. Plast. 154, 103294.
- Ming, K., Bi, X., Wang, J., 2018. Realizing strength-ductility combination of coarse-grained Al0.2Co1.5CrFeNi1.5Ti0.3 alloy via nano-sized, coherent precipitates. Int. J. Plast. 100, 177–191.
- Murr, L.E., 2015. Computer simulation in materials science and engineering. Murr, L.E. Handbook of Materials Structures, Properties, Processing and Performance. Springer International Publishing, Cham, pp. 1105–1121.
- Nie, J.F., 2003. Effects of precipitate shape and orientation on dispersion strengthening in magnesium alloys. Scr. Mater. 48, 1009-1015.
- Okayasu, M., Takeuchi, S., Matsushita, M., Tada, N., Yamasaki, M., Kawamura, Y., 2016. Mechanical properties and failure characteristics of cast and extruded Mg97Y2Zn1 alloys with LPSO phase. Mater. Sci. Eng. A 652, 14–29.
- Pan, F., Yang, M., Chen, X., 2016. A review on casting magnesium alloys: modification of commercial alloys and development of new alloys. J. Mate. Sci. Technol. 32, 1211–1221.
- Park, S.H., Lee, J.H., Moon, B.G., You, B.S., 2014. Tension-compression yield asymmetry in as-cast magnesium alloy. J. Alloys Compd. 617, 277-280.
- Peng, Q., Dong, H., Wu, Y., Wang, L., 2008. Age hardening and mechanical properties of Mg-Gd-Er alloy. J. Alloys Compd. 456, 395-399.
- Qiao, H., Guo, X.Q., Oppedal, A.L., El Kadiri, H., Wu, P.D., Agnew, S.R., 2017. Twin-induced hardening in extruded Mg alloy AM30. Mater. Sci. Eng. A 687, 17–27.
- Robson, J.D., 2014. Effect of rare-earth additions on the texture of wrought magnesium alloys: the role of grain boundary segregation. Metall. Mater. Trans. A 45, 3205–3212.
- Rokhlin, L.L., 2003. Magnesium Alloys Containing Rare Earth metals: Structure and Properties. Crc Press.

- Sandlöbes, S., Pei, Z., Friák, M., Zhu, L.F., Wang, F., Zaefferer, S., Raabe, D., Neugebauer, J., 2014. Ductility improvement of Mg alloys by solid solution: ab initio modeling, synthesis and mechanical properties. Acta Mater. 70, 92–104.
- Shahbeigi Roodposhti, P., Sarkar, A., Murty, K.L., 2015. Microstructural development of high temperature deformed AZ31 magnesium alloys. Mater. Sci. Eng. A 626, 195–202.
- Stanford, N., Atwell, D., Beer, A., Davies, C., Barnett, M.R., 2008. Effect of microalloying with rare-earth elements on the texture of extruded magnesium-based alloys. Scr. Mater. 59, 772–775.
- Stanford, N., Phelan, D., 2010. The formation of randomly textured magnesium alloy sheet through rapid solidification. Acta Mater. 58, 3642-3654.
- Takeuchi, A., Inoue, A., 2005. Classification of bulk metallic glasses by atomic size difference, heat of mixing and period of constituent elements and its application to characterization of the main alloving element. Mater. Trans. 46, 2817–2829.
- Wang, J., Zhang, J., Zong, X., Xu, C., You, Z., Nie, K., 2015. Effects of Ca on the formation of LPSO phase and mechanical properties of Mg-Zn-Y-Mn alloy. Mater. Sci. Eng. A 648, 37–40.
- Wang, Q., Chen, J., Zhao, Z., He, S., 2010. Microstructure and super high strength of cast Mg-8.5Gd-2.3Y-1.8Ag-0.4Zr alloy. Mater. Sci. Eng. A 528, 323-328.
- Wang, Q., Li, Z., Pang, S., Li, X., Dong, C., Liaw, P.K., 2018. Coherent precipitation and strengthening in compositionally complex alloys: a review. Entropy 20 (Basel). Wei, K., Hu, R., Yin, D., Xiao, L., Pang, S., Cao, Y., Zhou, H., Zhao, Y., Zhu, Y., 2021. Grain size effect on tensile properties and slip systems of pure magnesium. Acta Mater. 206.
- Wei, X., Cao, X., Luan, J.H., Jiao, Z.B., Liu, C.T., Zhang, Z.W., 2022. Synergy of strengthening and toughening of a Cu-rich precipitate-strengthened steel. Mater. Sci. Eng. A 832. 142487.
- Williamson, G.K., Hall, W.H., 1953. X-ray line broadening from filed aluminium and wolfram. Acta Mater. 1, 22-31.
- Williamson, G.K., Smallman, R.E., 1956. III. Dislocation densities in some annealed and cold-worked metals from measurements on the X-ray debye-scherrer spectrum. Philos. Mag. 1, 34–46.
- Wu, G., Wang, C., Sun, M., Ding, W., 2021. Recent developments and applications on high-performance cast magnesium rare-earth alloys. J. Magnes. Alloy 9, 1–20. Xie, D., Lyu, Z., Fan, M., Chew, H.B., Liaw, P.K., Bei, H., Zhang, Z., Gao, Y., 2021. Micromechanical origin of the enhanced ductility in twinless duplex Mg–Li alloy. Mater. Sci. Eng. A 815, 141305.
- Xie, D., Zhang, W., Lyu, Z., Liaw, P.K., Tran, H., Chew, H.B., Wei, Y., Ren, Y., Gao, Y., 2022. Plastic anisotropy and twin distributions near the fatigue crack tip of textured Mg alloys from in situ synchrotron X-ray diffraction measurements and multiscale mechanics modeling. J. Mech. Phys. Solids 165, 104936.
- Xu, D., Han, E.-h., Xu, Y., 2016. Effect of long-period stacking ordered phase on microstructure, mechanical property and corrosion resistance of Mg alloys: a review. Prog. Nat. Sci. Mater. 26, 117–128.
- Xu, S.S., Li, J.P., Cui, Y., Zhang, Y., Sun, L.X., Li, J., Luan, J.H., Jiao, Z.B., Wang, X.L., Liu, C.T., Zhang, Z.W., 2020. Mechanical properties and deformation mechanisms of a novel austenite-martensite dual phase steel. Int. J. Plast. 128, 102677.
- Xu, S.S., Zhao, Y., Chen, D., Sun, L.W., Chen, L., Tong, X., Liu, C.T., Zhang, Z.W., 2019. Nanoscale precipitation and its influence on strengthening mechanisms in an ultra-high strength low-carbon steel. Int. J. Plast. 113, 99–110.
- Yang, M., Pan, Y., Yuan, F., Zhu, Y., Wu, X., 2016. Back stress strengthening and strain hardening in gradient structure. Mater. Res. Lett. 4, 145–151.
- Yang, X., Wu, S., Lü, S., Hao, L., Fang, X., 2017. Effects of Ni levels on microstructure and mechanical properties of Mg-Ni-Y alloy reinforced with LPSO structure. J. Alloys Compd. 726, 276–283.
- Zhang, D., Yang, Q., Guan, K., Li, B., Wang, N., Qin, P., Jiang, B., Sun, C., Qin, X., Tian, Z., Cao, Z., Meng, J., 2019. A high-strength low-rare-earth-alloyed magnesium alloy via traditional hot-extrusion. J. Alloys Compd. 810, 151967.
- Zhang, D., Zhang, D., Bu, F., Li, X., Li, B., Yan, T., Guan, K., Yang, Q., Liu, X., Meng, J., 2017a. Excellent ductility and strong work hardening effect of as-cast Mg-Zn-Zr-Yb alloy at room temperature. J. Alloys Compd. 728, 404–412.
- Zhang, J., Xi, G., Wan, X., Fang, C., 2017b. The dislocation-twin interaction and evolution of twin boundary in AZ31 Mg alloy. Acta Mater. 133, 208-216.
- Zhang, J., Zhang, X., Li, W., Pan, F., Guo, Z., 2010. Partition of Er among the constituent phases and the yield phenomenon in a semi-continuously cast Mg–Zn–Zr allov. Scr. Mater. 63, 367–370.
- Zhang, J.Y., He, Q.F., Li, J., Yang, Y., 2021a. Chemical fluctuation enabling strength-plasticity synergy in metastable single-phase high entropy alloy film with gigapascal yield strength. Int. J. Plast. 139, 102951.
- Zhang, L., Zhang, J., Leng, Z., Liu, S., Yang, Q., Wu, R., Zhang, M., 2014. Microstructure and mechanical properties of high-performance Mg-Y-Er-Zn extruded alloy. Mater. Des. 54, 256–263, 1980-2015.
- Zhang, S.-.Y., Wang, C., Ning, H., Wang, T., Zhang, C.-.C., Yang, Z.-.Z., Wang, H.-.Y., 2021b. Relieving segregation in twin-roll cast Mg-8Al-2Sn-1Zn alloys via controlled rolling. J. Magnes. Alloy 9, 254–265.
- Zhao, Y.L., Yang, T., Tong, Y., Wang, J., Luan, J.H., Jiao, Z.B., Chen, D., Yang, Y., Hu, A., Liu, C.T., Kai, J.J., 2017. Heterogeneous precipitation behavior and stacking-fault-mediated deformation in a CoCrNi-based medium-entropy alloy. Acta Mater. 138, 72–82.
- Zhu, J., Chen, X.H., Wang, L., Wang, W.Y., Liu, Z.K., Liu, J.X., Hui, X.D., 2017. High strength Mg-Zn-Y alloys reinforced synergistically by Mg12ZnY phase and Mg3Zn3Y2 particle. J. Alloys Compd. 703, 508–516.